MNE 20 (2023) 100224

Contents lists available at ScienceDirect

Micro and Nano Engineering

journal homepage: www.sciencedirect.com/journal/micro-and-nano-engineering

3D-printed microfluidic system for the *in situ* diagnostics and screening of nanoparticles synthesis parameters

V.V. Shapovalov [a,*], S.V. Chapek [a], A.A. Tereshchenko [a], A.N. Bulgakov [a], A.P. Bagliy [a,b], V.V. Volkov [c], P.V. Konarev [c], M.A. Soldatov [a], S.A. Soldatov [a], A.A. Guda [a,*], A.V. Soldatov [a]

[a] *The Smart Materials Research Institute, Southern Federal University, 344090 Rostov-on-Don, Russia*
[b] *Institute of Mathematics, Mechanics and Computer Science, Southern Federal University, 344090 Rostov-on-Don, Russia*
[c] *A.V. Shubnikov Institute of Crystallography, Federal Scientific Research Centre "Crystallography and Photonics", Russian Academy of Sciences, 119333 Moscow, Russia*

ARTICLE INFO

Keywords:
3D-printed microfluidics
Reaction parameters screening
Ag nanoparticles
Machine learning
UV–Vis spectroscopy
Small-angle X-ray scattering

ABSTRACT

Fine tuning of the material properties requires many trials and errors during the synthesis. The metal nanoparticles undergo several stages of reduction, clustering, coalescence and growth upon their formation. Resulting properties of the colloidal solution thus depend on the concentrations of the reagents, external temperature, synthesis protocol and qualification of the researcher determines the reproducibility and quality. Automatized flow systems overcome the difficulties inherent for the conventional batch approaches. Microfluidic systems represent a good alternative for the high throughput data collection. The recent advances in 3D-printing made complex topologies in microfluidic devices cheaper and easily customizable. However, channels of the cured photopolymer resin attract metal ions upon synthesis and create crystallization centers. In our work we present 3D-printed system for the noble metal nanoparticle synthesis in slugs. Alternating flows of oil and aqueous reaction mixtures prevent metal deposition on the channel walls. Elongated droplets are convenient for optical and X-ray diagnostics using conventional methods. We demonstrate the work of the system using Ag nanoparticles synthesis for machine-learning assisted tuning of the plasmon resonance frequency.

1. Introduction

Noble metal nanoparticles (NPs) find a wide range of industrial applications, including catalysis, photonics, drug delivery, medical imaging. Their unique optical properties are interesting for surface-enhanced Raman scattering, photovoltaics, molecular detection, and photothermal cancer therapies [1,2]. In a typical procedure metal nanoparticles grow in the presence of metal ions, reducing agent and stabilizer [3]. The result of the reduction, nucleation and growth depends on many parameters, including temperature and reagent concentrations. The human operator may unintentionally introduce variations in standard protocols by varying mixing time or speed and order of reagents that affect the resulting particle size distribution [4]. Design of experiments approach may help to identify the role of each synthesis parameter on the resulting properties [5–7] while machine learning (ML) algorithms offer a more sophisticated alternative that is capable to find complex dependencies in the highly dimensional data and apply optimization strategies [8–10]. Several examples in the literature demonstrate successful application of the ML models to find relationships between the synthesis and material properties. Dong et al. has addressed the relationships among initial reactant concentration, ultrasound intensity, and average particle size of Ag NPs [11] by means of decision trees algorithm. Li et al. applied data-driven approach to accelerate the synthesis of small gold nanoclusters [12], while Zhao et al. combined literature data mining and robotic platform for reproducible screening of colloidal nanocrystals synthesis [13]. The deep learning algorithm incorporated all parameters in the synthesis into consideration and helped to understand complex inorganic material synthesis. Wahl et al. presented a ML–driven optimization for the synthesis of polyelemental metal nanoparticles with targeted structural properties [14]. Pellegrino et al. showed that trained models can be applied for reverse engineering approach [15] to find the optimal synthesis parameters for a desired characteristic of TiO_2 NPs.

Classical synthesis routines are often limited to a few numbers of samples due to high amount of reagent consumption, while also having complex parallelization and reproducibility issues. Flow chemistry and

* Corresponding authors.
E-mail addresses: viks@sfedu.ru (V.V. Shapovalov), guda@sfedu.ru (A.A. Guda).

https://doi.org/10.1016/j.mne.2023.100224
Received 27 April 2023; Received in revised form 7 July 2023; Accepted 5 August 2023
Available online 7 August 2023

microfluidics, on the contrary, provide unique possibilities for precise control over mixing and heat transfer in tiny reagent volumes [16,17]. This approach allows to build highly customized and efficient systems for nanomaterial synthesis. Microfluidic approach also offers a powerful alternative to the batch synthesis in terms of online monitoring analytics and self-optimization [18–20]. For this purpose, microfluidic system must be coupled with a robust and efficient methods for diagnostics. Being sensitive to the localized surface plasmon resonance (LSPR) effect of noble metal nanoparticles, UV–Vis spectroscopy is particularly noteworthy [21,22]. The parameters of the absorption spectrum depend on both size and shape of nanoparticles, and wavelength of the plasmon resonance may vary across the visible range from 400 nm to near-infrared region at 1100 nm [23,24]. This makes the optical spectroscopy a perfect technique for laboratory characterization of nanoparticles. Nguyen et al. developed a microfluidic serial centrifuge and employed UV–Vis absorption spectroscopy for efficient screening of Au nanoparticles synthesis [25]. Yang et al. applied UV–Vis spectroscopy to characterize Ag nanoparticles produced in different regimes by their novel multi-stage microfluidic reactor with integrated valveless piezoelectric pumps [26]. Thanks to the sensitivity and speed of the optical spectroscopy it can be applied is situ for on-line tracking of noble metal nanoparticle growth, especially when combined with ML-based optimization algorithms [27,28]. Mekki-Berrada developed two-step framework for a machine learning-driven high-throughput microfluidic platform to rapidly produce silver nanoparticles with the desired UV–Vis absorbance spectrum [29]. They combined deep neural network to approximate the spectrum as a function of synthesis parameters and Bayesian optimization to guide the microfluidic system. Existing works in the literature address also the ML-assisted microfluidic synthesis of quantum dots [6,30] and perovskites [31].

Synchrotron X-ray scattering based techniques are another family of methods that allow *in situ* characterization of nanoparticle growth in microfluidic chips [32,33]. Radajewski et al. used simultaneous collection of wide- and small-angle X-ray scattering data (WAXS/SAXS) to investigate the magnetite nanoparticles growth in droplet microreactor. A two-step data processing technique was employed, where WAXS data were used to select frames with droplets to further analyze their SAXS patterns [34]. Lange et al. demonstrated that using highly X-ray transparent and low-scattering material, such as off-stoichiometric thiol-ene-epoxy it is possible to investigate the chemical processes right inside the microfluidic device (MFD). The example applications included the SAXS study of gold nanoparticles segmented flow in water droplets, the liquid/liquid extraction of cerium oxalate in the oil phase, and WAXS study of cerium oxalate crystals synthesized in a binary water/propanediol solvent [35].

Current methods to produce microfluidic devices involve micromachining, hot embossing, etching and molding [36–38]. However, these processes can be time consuming, imprecise, expensive or challenging to produce complex channel topologies. Moreover, some of them also require clean-rooms and other facilities to ensure error-free devices, which are often expensive to build and maintain. This is where additive manufacturing comes into play with its accessibility and reliability. One of the most robust and versatile 3D-printing technology that could be used is digital light processing stereolithography (DLP-SLA) [39–41]. The benefits of using 3D-printed microfluidic devices for synthesis are demonstrated in recent reviews [42,43]. Guda et al. employed a system of 3D-printed microfluidic devices for *in situ* screening of UV-mediated Au nanoparticles synthesis [44]. Van der Linden et al. demonstrated the ability of the DLP-SLA technology to produce complex 3D microchannel topologies, otherwise hard or near impossible to achieve with conventional fabrication methods [45]. Simple, cheap yet efficient microfluidic device, manufactured with hybrid PDMS/3D-printing technology, was reported by Bressan et al. The device is suitable for the flow synthesis of Ag and Au nanoparticles [46]. Camarillo-Escobedo et al. developed a 3D-printed MFD with integrated spectrophotometer and wireless connectivity, and demonstrated its application for the analysis of fluoride content in ground waters [47].

One of the drawbacks of the 3D-printed systems is the presence of non-passivated functional groups on the surface of cured resin. The channels of the 3D-printed chip attract the metal ions and create additional nucleation and growth centers upon synthesis. The synthesis in water-in-oil droplets helps to overcome this issue with a cost needed to synchronize droplet flow and spectral characterization, that often may lead to unacceptable quality of the data. In this work we demonstrate a combination of microfluidic approach and *in situ* diagnostics applied to automated synthesis of Ag nanoparticles in a slug flow. The slugs represent a good compromise for an isolated microreactor with customizable length optimal for UV–Vis and X-ray characterization. The reagent mixing, slug volume and timing are adjusted in a modular system comprised of 3D-printed microfluidic devices. The UV–Vis absorption data collected during the screening enabled to train ML models and visualize optimal conditions for synthesizing nanoparticles with specific properties. This approach can be easily adapted and scaled for various microfluidics-based reactions. The integration of the microfluidics and artificial intelligence technologies will greatly accelerate the development of new functional nanomaterials and significantly improve the efficiency of research.

2. Methods

2.1. Microfluidic system

All microfluidic devices were designed in Fusion 360 (Autodesk, USA) and 3D-printed with a FunToDo Nano Clear (Alkmaar, Netherlands) resin on an Asiga MAX UV (Sydney, Australia) DLP-SLA 3D-printer. At 25 μm layer thickness the printing time for an 8 mm thick MFD was typically 40 min. After printing, the devices were removed from the build plate and sonicated in IPA for 90 s at 50 kHz and 35 W power, following with the manual flushing of the channels with isopropyl alcohol. MFDs were then blown dry with compressed air, based on existing post-processing protocol [45]. After drying the channels of MFDs were filled with vaseline oil and left overnight to improve the surface hydrophobicity.

A set of Wingflow Qmix-HZ 90 (Wingflow AG, Frick, Switzerland) syringe pumps with borosilicate glass syringes was used to precisely control the flow of reactants and carrier phase. Standard 1/4″-28 UNF flangeless PTFE connectors and PFA tube (1/32″ ID) was used to connect individual parts of the microfluidic system. Medical grade PVC infusion tube (1.5 mm ID) was used for the delay line.

2.2. Synthesis and experiment control

Aqueous solutions of silver nitrate $AgNO_3$, trisodium citrate (Na_3Cit) $Na_3C_6H_5O_7$, and L-ascorbic acid (AA) $C_6H_8O_6$ prepared from commercial powders (Sigma Aldrich) at concentrations of 2 mM, 6 mM, and 12 mM, respectively, were used as components of the reaction mixture and supplied to the inputs 1–3 of the slug generator. The system of syringe pumps, performing dosing of reaction mixture components, was controlled from PC. The control algorithm subdivided the space of reaction parameters into a set of experimental points according to the improved distributed hypercube sampling (IHS) method, which is an advanced sampling technique allowing to get well-distributed sample sets with uniform and complete coverage of the multidimensional parameter space using a relatively small number of samples [48]. The control algorithm then performed automatic transition between these points and collected spectroscopy data according to a preset program.

2.3. Characterization of Ag nanoparticles

In situ UV–Vis absorption spectra were acquired using the OceanFX fiber optic UV–Vis spectrometer (Ocean Insight, Orlando, USA) with 35 ms integration time and 100 ms acquisition interval. Xe arc lamp setup

was used as a light source. During measurements, dark and background signal were subtracted automatically, as well as the reference signal of pure vaseline oil.

SAXS data was acquired at the BioMUR beamline of the NRC "Kurchatov Institute" synchrotron facility [49] using 8.58 keV (λ = 1.445 Å) radiation. Scattering patterns were collected using Pilatus 3 1 M (Dectris AG, Baden-Daetwill, Switzerland). To avoid air scattering 2500 mm long vacuum chamber was installed between the sample and the detector. The sample to detector distance and wavelength were calibrated using Ag behenate standard. SAXS patterns were acquired in the scattering vector range s = 0.0015 to 2.75 nm^{-1} ($s = 4\pi\sin(\theta)/\lambda$, where 2θ — scattering angle). For *in situ* study characterization in segmented flow the exposure time for each pattern was 1 s and patterns were collected continuously for 300 s. For IHS validation measurements 8 images with 60 s acquisition time were collected for each point. Acquired images were radially integrated using Fit2D software [50] and resulting 1D scattering patterns were normalized by the exposure time and storage ring current, then the background signal from the vaseline oil in a cuvette or tube was subtracted. Particle size distributions were restored by the program MIXTURE from the ATSAS package [51] in the scattering vector range s = 0.04 to 0.8 nm^{-1} using a model of two-component polydisperse spheres. Each component was described by its volume fraction, the average particle size and degree of polydispersity according to the Schulz distribution function.

TEM images were acquired on a Tecnai G2 Spirit TWIN (FEI, Netherlands) transmission electron microscope using an accelerating voltage of 80 kV and Cu meshes as sample supports. To analyze the particle size distribution the images were processed in the ImageJ software (Version 1.54d, National Institutes of Health, Bethesda, MD, USA) [52]. For each sample over 300 particles were analyzed to achieve better statistics, and the average between the minimum and maximum Feret diameter was considered as the particle size [53].

2.4. Machine learning

We have studied relationships between synthesis parameters and optical properties of resulting colloidal solution. To reduce effects of noise and background subtraction we applied dimensionality reduction on the input data and calculated two descriptors of spectrum – intensity and position of the plasmon resonance peak. The Extra Trees ML algorithm was trained on the dataset [synthesis parameters, descriptors of spectrum]. Extra trees [54] is a general-purpose nonlinear regressor. This method is suitable for large dimensional problems with a small number of samples. Extra Trees method constructs a piecewise-linear approximation. It combines the predictions of multiple decision trees and demonstrates better performance compared to other ensemble tree algorithms. Unlike Random forest, the Extra trees uses the whole training sample and chooses the cut points for splitting randomly. These differences allow Extra trees to reduce bias and variance of predictions. Extra trees implementation is used as a part of the scikit-learn package [55]. In particular, we use the function sklearn.ensemble.ExtraTreesRegressor with arguments n_estimators = 40, min_samples_leaf = 1, max_depth: unlimited; min_samples_split: 2; bootstrap: False, as implemented in PyFitIt software [56].

The quality of approximation was calculated *via* the leave-one-out cross-validation (LOOCV) method. In statistics and in the field of machine learning, the R^2 *score*, or the coefficient of determination, is a popular quality measure. Let y_i and f_i ($i = 1,..,n$) be the exact and the predicted values of unknown function and m the mean of y_i, then R^2 *score* is defined

$$R^2\ score = 1 - \frac{\sum (y_i - f_i)^2}{\sum (y_i - m)^2} \quad (1)$$

The maximum value $R^2\ score = 1$ corresponds to the best possible prediction, *i.e.* $f_i = y_i$. In practice, R^2 *score* can be 0 and even negative, for badly trained or overfitted models. Another important metric used for summarizing and assessing the quality of a machine learning model is the *mean absolute error (MAE)* of prediction, with is calculated as the sum of absolute errors (differences between the true value and predicted) divided by the sample size:

$$MAE = \frac{\sum |y_i - f_i|}{n} \quad (2)$$

3. Results

3.1. 3D-printed microfluidic system

The developed system includes a combination of microfluidic devices consisting of a slug generator chip, slug spacer chip, delay line and a flow cell for the chosen characterization technique (Fig. 1). 3D models of the microfluidic devices can be found in the SI for this paper.

In a typical setup, the reactants are supplied to the inputs of the droplet generator, while another input is supplied with the carrier phase. The generator forms a flow of reaction mixture droplets in the carrier phase, where each droplet acts as a separate chemical microreactor. The droplet size and frequency can be adjusted by varying the rate and ratio of reactant and carrier phase flows. The droplet flux in the carrier phase is connected from the generator output to the spacer input. The carrier phase is additionally supplied by a separate syringe pump to the spacer to be added between the droplets in the structured flow, thus increasing the distance between them (see Fig. 2a). The droplet stream from the spacer outlet then enters a delay line that allows to adjust the reaction time. The delay line connected to a specially designed *in situ* flow cell, suitable for selected diagnostics method.

Fig. 2b shows the UV–Vis *in situ* flow cell. Its body (1) has a 600 μm thick U-shaped capillary channel, with the ends of its straight section closed by 1 mm quartz glass windows (2). Two optical fibers from the UV–Vis spectrometer are brought to the windows and secured in special holders (3). Such a setup allows the transmission measurement of optical absorption spectra from the solutions in slugs as they move through the cell. The size of water phase slugs (green in Fig. 2a) is adjusted in a way that they can completely fill the straight part of the capillary in the cell.

3.2. Screening the relationships between plasmonic properties and synthesis parameters

We performed automated screening of synthesis parameters to fine-tune the LSPR effect of Ag nanoparticles. Individual reagent flow rates for silver nitrate and trisodium citrate were varied ranging from 0.75 to 3.375 mL/h, the L-ascorbic acid flow at each experiment point was adjusted so that the total reagent flow during synthesis was 7.5 mL/h. Vaseline oil was supplied to the fourth inlet of the droplet generator as a carrier phase at 4 mL/h, and it was also supplied to the spacer using an additional pump at 8 mL/h. Based on the observed slug length of 4-4.5 mm in the tube with known ID of 1.5 mm, we can estimate the water phase slug volume where NPs were synthesized to be 7-8 μL. The reaction was studied at the temperatures of 25 and 60 °C with reaction time of 7 min. The temperature of 25 °C represents the normal ambient conditions, however, the thermostat was still used to avoid any temperature fluctuations as microfluidic systems can be very sensitive to them. For elevated temperature synthesis the temperature of 60 °C was selected as it is the highest temperature at which there is no boiling in the water phase. At higher temperature vapor bubbles start to form actively in the water phase slugs which disrupts the slug flow and *in situ* UV–Vis measurements. A coiled capillary tube immersed in a thermostat (water bath) was added between the spacer and the *in situ* cuvette, acting as a delay line. 47 sets of flow values were generated by IHS (see Table S1), and for each set the system automatically produced microdroplets with the corresponding reactant flows for 1 min and continuously gathered UV–Vis absorption spectra. Since it takes 7 min for

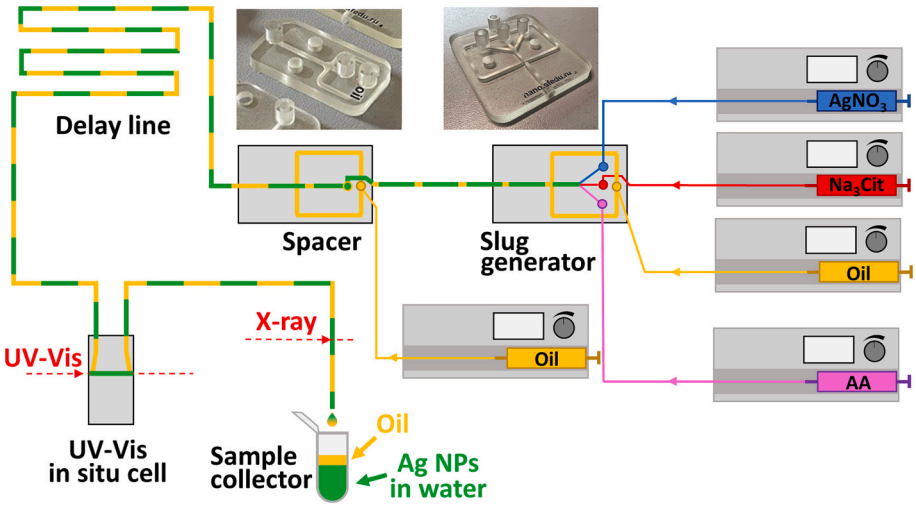

Fig. 1. Experimental setup consisting of the set of syringe pumps, slug flow generator chip, slug spacer chip, delay line, *in situ* UV–Vis cell and sample collector.

droplets to pass through the delay line, by the time the first batch of droplets reaches the cuvette, six more batches with different parameters are traveling in the delay line. Custom software was used for filtering out data from the oil only and oil-droplet boundaries, and for consequent matching of the spectra obtained from individual droplets with the synthesis parameters in these droplets. Keeping in mind that each flow combination was tested at 2 different temperatures, the employed scheme allowed to test and characterize 100 sets of synthesis conditions in <2 h.

Fig. 3 shows several spectra obtained for different ratios of reactant fluxes and at different reaction temperatures. The spectra clearly show differences in the position and intensity of the plasmon resonance peaks, indicating differences in the size distribution and concentration of silver nanoparticles obtained during the synthesis. At the same time, the plasmon resonance peaks in the case of synthesis at a higher temperature have a generally smaller width, which indicate a narrower size distribution of nanoparticles and lower polydispersity.

The resulting data indicates reproducible relationships between reagent flows and spectral response of the resulting colloidal solution. As follows from Fig. 4a,c the plasmon resonance position shifts towards lower wavelength (pink background color in the figure) at lower Ag concentration. The lowest position is observed in the excess of ascorbic acid. At higher flow rates of Ag precursor the plasmon resonance shifts towards higher wavelength, indicating larger sizes of nanoparticles [57,58]. The largest shift is observed at near stoichiometric Ag:AA ratios.

Intensity of the plasmon resonance depends on the concentration of formed Ag nanoparticles in the solution and dispersion in their sizes. The former is proportional to the flow of the Ag precursor. Ascorbic acid is needed to reduce the Ag ions and in Fig. 5 we observe optimal region in the center of the map where intensity reaches maximum. At lower values of AA the intensity decreases due to presence of unreduced ions. While at higher values of AA flow the resulting particles may sediment and appear to have larger polydispersity. The process of noble metal NPs formation is known to be highly dependent on the pH value of reaction mixture [59,60]. Overall acidity of the reaction mixture and fast introduction of excess amounts of AA boosts the agglomeration of small nanoparticles [57,61]. This process is further aggravated with the relatively large volume of droplet microreactors and their slow movement, which also favors the growth of larger Ag nanoparticles [62,63]. Low pH also provides disbalance between the nucleation and growth processes, thus making it difficult to obtain stable spherical monodisperse nanoparticles [64].

The set of descriptors of spectra was further analyzed using machine learning methods to obtain a model predicting the surface plasmon properties of Ag nanoparticles based on the synthesis conditions. The flow rates of the reactants were chosen as variable parameters, while the position and intensity of the plasmon resonance peak (see fig. S3) were chosen as spectral descriptors for prediction. Figs. 4a,c and 5a,c show the results of the ML model training on the basis of experimental points (represented as white circles). The model was then applied to predict value of LSPR peak intensity and position at any point of the parameters space. The prediction result is represented by the background color of the 2d-map. The obtained models were cross-validated (Figs. 4b,d and 5b,d) using leave-one-out scheme and checked for consistency with the experimental data and found to be highly reliable (determination coefficient R^2 score ≥ 0.84 and MAE ≤ 3.8 nm for LSPR peak position and $\leq$ 0.1 a.u. for peak intensity). The higher value of the coefficient and lower MAE for the synthesis at 60 °C indicates narrower distribution of the characteristics of silver nanoparticles formed at this temperature, as elevated temperature promotes the reduction activity of trisodium citrate.

3.3. *Relationships between synthesis parameters and nanoparticles sizes studied by SAXS*

The long slugs with sufficient spacing between them make the microfluidic system applicable for conventional spectroscopic studies at laboratory and synchrotron sources. We applied *in situ* synchrotron SAXS to study time-dependence of the Ag NP growth. For this, 1 mm internal diameter PFA tube was added after the spacer chip. The SAXS signal was measured trough this tube perpendicular to the flow, and by changing the distance from the spacer to the measurement spot we were able to vary the time from the reaction start to the product characterization. Individual flow rates for all reactants were set equal to 4 mL/h, and vaseline oil flow was set to 2.5 mL/h for both the droplet generator and spacer.

The SAXS patterns were measured continuously from the slug flow in the tube. Then, among all measured patterns, the scattering curves obtained from the aqueous phase droplets containing Ag NPs (red curves in Fig. 6) were selected, normalized by the storage ring current, averaged, and background was subtracted. The obtained curves are shown in Fig. 7. Resulting size distribution is bimodal. The average particle size in the model of two-component polydisperse spherical particles was subsequently determined for them (Table 1). As a result, at the tube length of 8 cm (reaction time ~ 10 s) there were no Ag NPs observed, but when the tube length was increased to 40 cm (reaction time ~ 48 s), a significant number of Ag particles with an average radius of about 6 nm and a smaller number of larger particles with a radius of 20 nm are observed. With further increase in the tube length, the fraction of larger particles

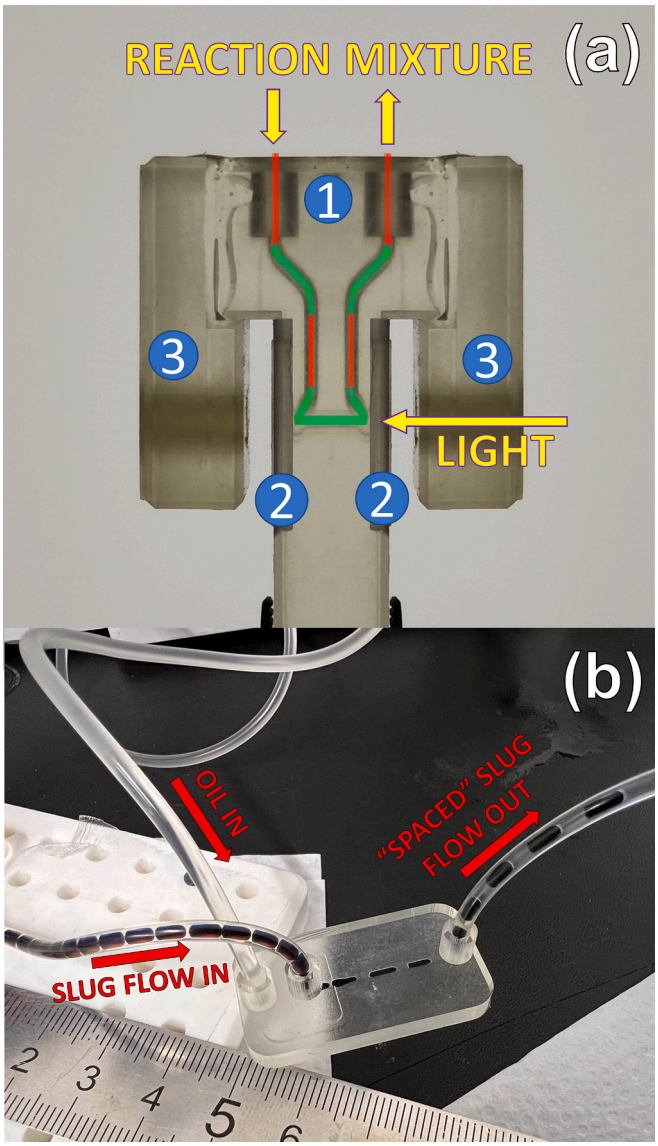

Fig. 2. (a) View of the flow cell for *in situ* UV–Vis spectroscopy, consisting of the cell body (1), quartz windows (2), and optical fiber holders (3). Red and green colors represent, respectively, oil and water phases in a slug flow through the cell. (b) Spacer chip in work, increasing the distance between individual droplets in a slug flow of a model dye solution. (For interpretation of the references to color in this figure legend, the reader is referred to the web version of this article.)

(denoted as "Phase 1" in Table 1) increases, and their average size also increases. We found that resulting size distribution does not vary dramatically at tube length above 1 m that corresponds to the reaction time of ~120 s. Thus approximately 2 min is sufficient for the initial rapid nucleation and growth stages, and further aging and agglomeration occurs slowly afterwards. Compared to some 7–15 min (and longer) Ag NP synthesis by AA reduction, reported in batch protocols [57,58,61], this proves the efficiency of microfluidic approach and its positive effect on reaction kinetics.

The size distribution of the resulting nanoparticles was further screened *via* IHS approach and SAXS data to study the impact of different reactant flow rates on Ag NP growth and resulting phase concentrations. 15 combinations (Table 2) of flows rate were selected as described in SI. The resulting scattering patterns (Fig. S2) were approximated with the model of two-component polydisperse spherical particles to obtain data on the average particle radius and the degree of

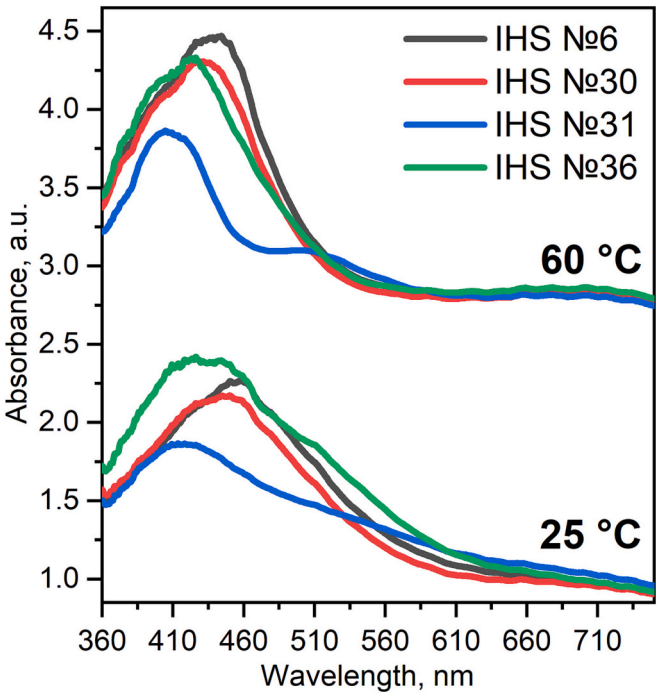

Fig. 3. Characteristic UV–Vis absorption spectra obtained for various combinations of reagent flows from Table S1 in case of the synthesis performed at 25 °C and 60 °C.

polydispersity. The fit quality was good as clear from Fig. S4. It was found that for all measured flow combinations two sizes of Ag particles were present - larger particles ("Phase 1") with an average radius of 16.6 to 30 nm, and smaller particles ("Phase 2") with an average radius of 3.2 to 6 nm. At the same time, the concentration of "Phase 1" was noticeably higher (70 to 98%).

Among all ratios tested, the largest particle size of coarser "Phase 1" (mean radius of 30 nm) was achieved in the case of IHS 8 with an $AgNO_3$:Na_3Cit:AA flow ratio of 0.8:0.9:5.8 mL/h, that is, with a significant excess of ascorbic acid acting as reducing agent. Meanwhile, as it follows from the Fig. 7, for near stoichiometric Ag:AA ratios (with a slight excess of the reducing agent) Ag NPs with high fraction of larger particles are mostly formed. When the silver precursor $AgNO_3$ was in excess (IHS 3, IHS 15) compared to the reducing agent (AA), the fraction of finer "Phase 2" increased. Those results correlate well with the models trained on *in situ* UV–Vis data. Low concentrations of $AgNO_3$ with balanced concentrations of the reducing and stabilizing agents are predicted to result in lowest LSPR wavelength, which means smallest nanoparticles, in agreement with the SAXS observations. At the same time, largest LSPR wavelength, thus, nanoparticle size, is predicted for the near stoichiometric flow combinations or with slight excess of the ascorbic acid, similar to the SAXS results. Those observations also agree with the literature data as described in the previous section.

3.4. TEM characterization of synthesized nanoparticles

To further validate the size and distribution of the nanoparticles, a series of TEM measurements were performed. 6 points were selected from the SAXS experiment (IHS 1, 3, 6, 8, 12 and 15 from Table 2). For these flow combinations the synthesis was repeated in the same microfluidic system using manual flow control. At the end of the delay line the sample was collected in a vessel. There, water phase containing Ag nanoparticles were naturally separating from the oil. Then, using a micropipette, droplets of water phase were deposited on Cu-meshes for TEM and left to dry overnight.

Fig. 8 shows the transmission electron microscopy images acquired

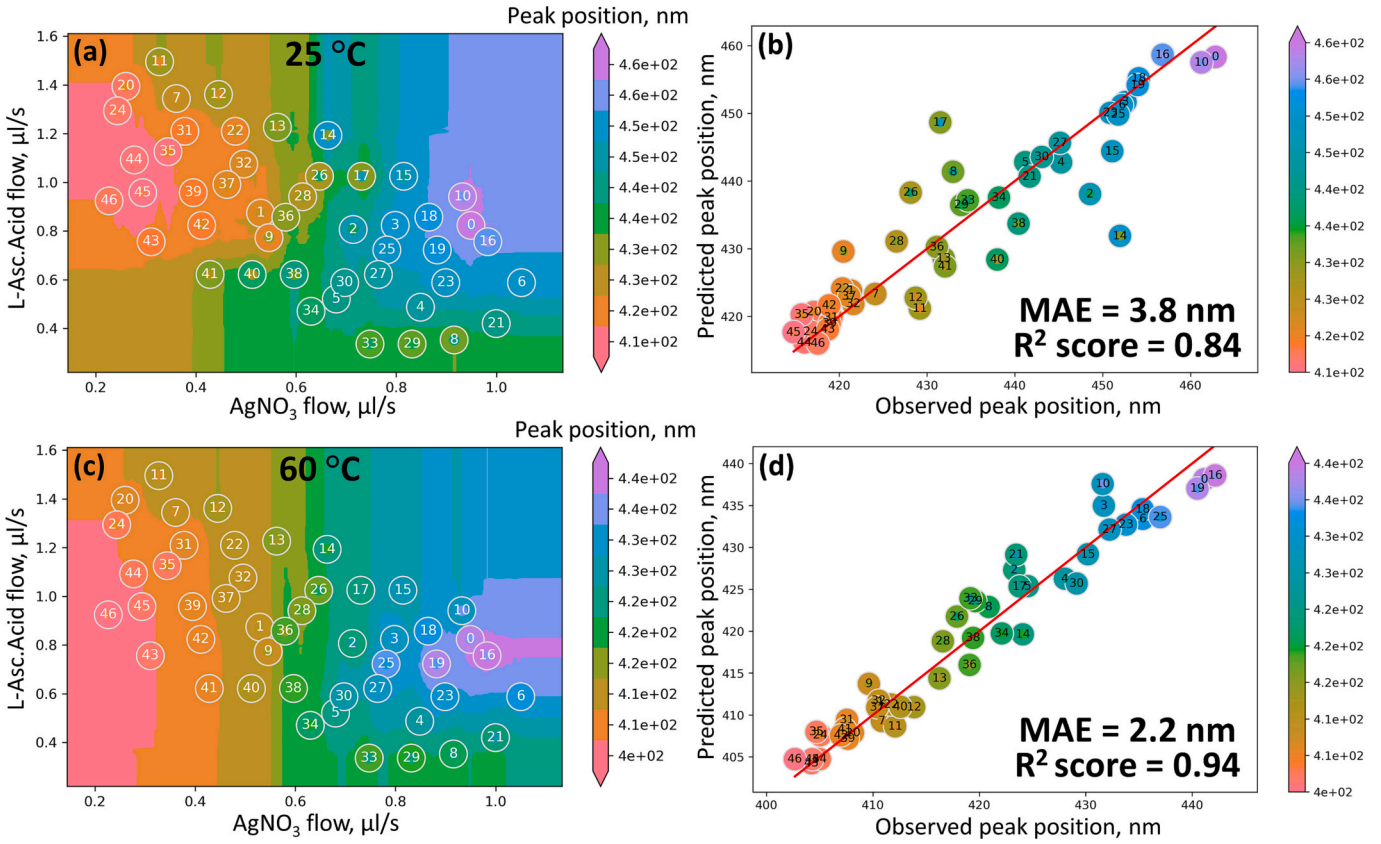

Fig. 4. Model predicting the LSPR peak position in the UV–Vis spectra of silver nanoparticles as a function of $AgNO_3$ and L-ascorbic acid flow rates for the synthesis at 25 °C (a) and 60 °C (c). Each white point is the result of a separate synthesis with parameters derived from IHS sampling (see Table S1 for details). The background color of the map represents the prediction results of the ML algorithm trained on experimental datapoints. Panels (b) and (c) show the result of the leave-one-out cross-validation for respective models.

from the synthesized nanoparticles. The images show substantial difference in both size and shape of the nanoparticles depending on the reactant flows. Despite the fact that the average Feret diameter distributions shown in Fig. 9 demonstrate in general higher particle size than suggested by SAXS, the general trend has reasonable agreement with the results of synchrotron diagnostics. For instance, the samples synthesized with the lack of reducing agent (in particular IHS12 and IHS15) demonstrate wide and somewhat bimodal size distribution (Fig. 9e-f), similar to SAXS, where substantial concentration of small particles and high polydispersity were observed for these samples. Those samples also had the lowest concentration of nanoparticles, with is observed in both TEM and low LSPR intensity in UV–Vis spectra of NPs synthesized with similar $AgNO_3$:AA flow ratios. On the contrary, synthesis with the excess of ascorbic acid results in larger particles, which is particularly notable for the sample IHS8 (Fig. 9d), where some of the largest particles reaching 60–70 nm were observed. Particle shape is also heavily affected by the synthesis conditions. In the baseline sample IHS1 (Fig. 8a) with reactants flows balanced 1:1:1, the particles are close to spherical with somewhat irregular shape and have the smoothest and the widest distribution of sizes. Whereas sample IHS6 (Fig. c), having the narrowest distribution, mostly consists of polyhedral or pyramidal particles with well-defined shape, with inclusions of some flat pancake-shaped particles. Sample IHS8 (Fig. 8d) contains even more of those flat particles with some quite large (up to 70 nm) Ag flakes. However, non-spherical polydisperse nanoparticles are to some extent to be expected as the synthesis was performed under sub-optimal pH values.

The major reason behind the overall difference in nanoparticle size distribution obtained from SAXS and TEM is likely the fact that the actual synthesis time for these 2 methods was inadvertently different. For SAXS experiment the measurements were performed on a freshly synthesized nanoparticles after consistent residence time in microfluidic system. Whereas in case of the TEM imaging, nanoparticles were first collected in batch without any additional stabilization and kept this way for ~10 min until separated from oil. Then droplets of several microliters in volume were placed on Cu meshes to evaporate overnight, effectively increasing the synthesis time to hours, which gave nanoparticles more time to grow and agglomerate.

4. Discussion

The optimization of nanoparticle synthesis in microfluidic systems encounters several challenges. First is the appropriate topology for mixing and reaction zones of the microfluidic devices. Second is the *in situ* diagnostics of the product. Application of 3D-printing to microfluidic device manufacturing systems offers a good alternative to glass, polydimethylsiloxane (PDMS) and poly(methyl methacrylate) (PMMA) chips. It enables quick and efficient optimization of the microfluidic device topology for various tasks. For example, it becomes possible to quickly obtain droplet generators with different numbers of reagent inlets, produce highly efficient micromixers with channel topologies fine-tuned for specific mixture properties. Low-cost 3D-printed microfluidic devices are perfect for laboratory application as they can be tuned for a specific experiment, used single time and thrown away, avoiding the risk of failure due to the MFD degradation or reactant cross-contamination. If the more prolonged use is required, however, the technology is perfect for the cost-efficient prototyping and optimization of microfluidic systems. Optimized 3D design then might be scaled for production and manufactured with more batch-efficient technologies and out of more resistant materials for the extended lifecycle. Such an approach allows to eliminate costly errors at the early prototyping stages

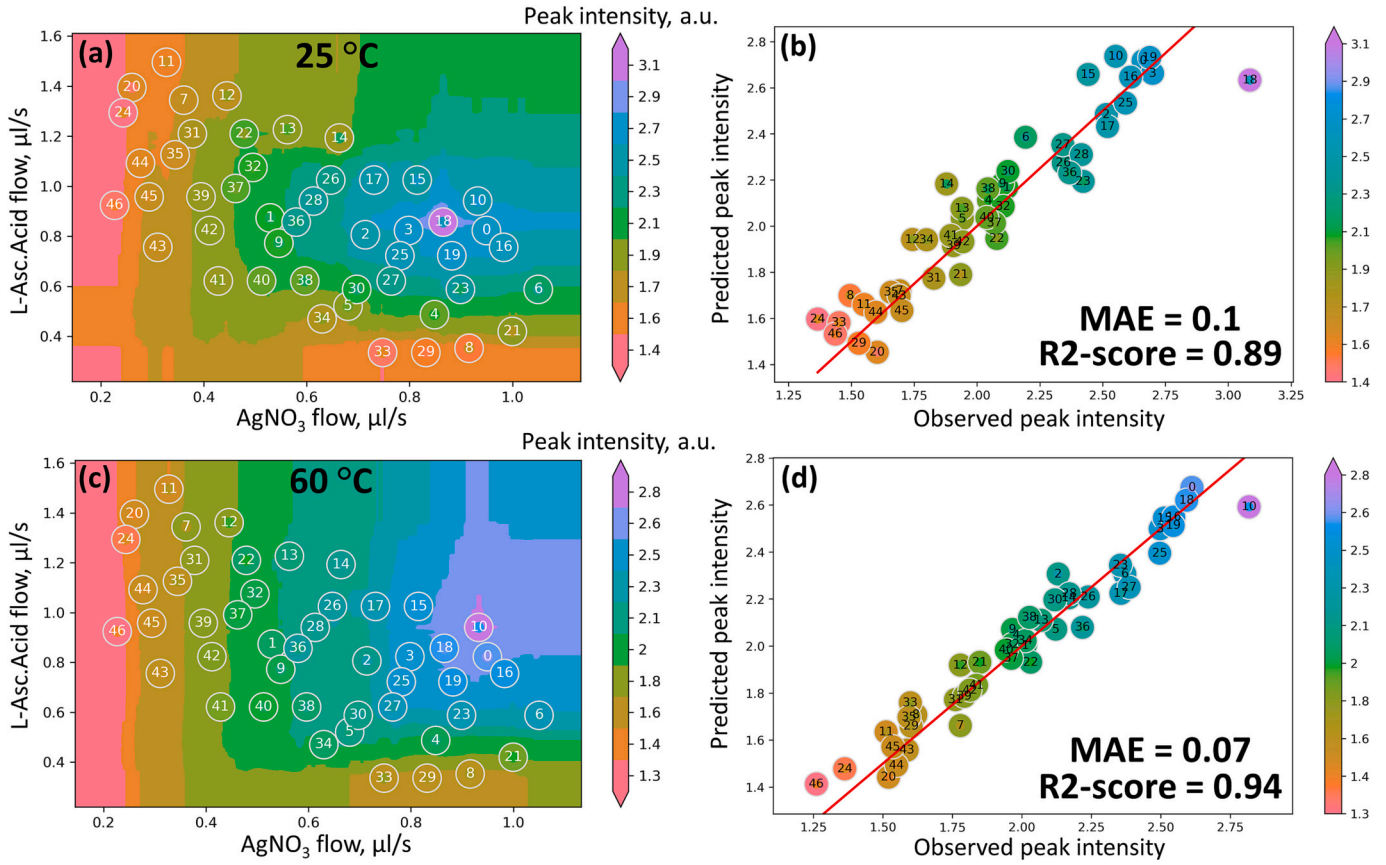

Fig. 5. Model predicting the LSPR peak intensity in the UV–Vis spectra of silver nanoparticles as a function of $AgNO_3$ and L-ascorbic acid flow rates for the synthesis at 25 °C (a) and 60 °C (c). Each white point is the result of a separate synthesis with parameters derived from IHS sampling (see Table S1 for details). The background color of the map represents the prediction results of the ML algorithm trained on experimental datapoints. Panels (b) and (c) show the result of the leave-one-out cross-validation for respective models.

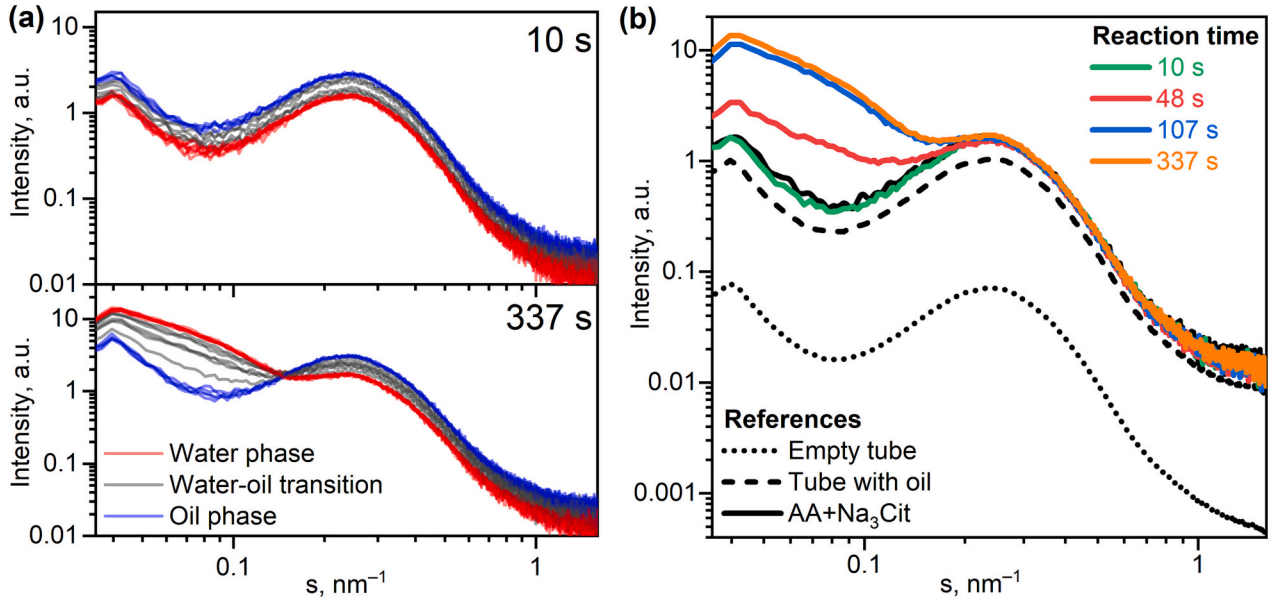

Fig. 6. (a) SAXS patterns measured from the alternating water-in-oil slog flow with 1 s acquisition time for 1 min. The generator chip to acquisition spot flow time of 10 and 337 s (indicated in the graph panel) corresponds to the delay line length of 8 and 278 cm, respectively; (b) Averaged SAXS patterns from slugs with Ag NPs, measured with different reaction delay line length.

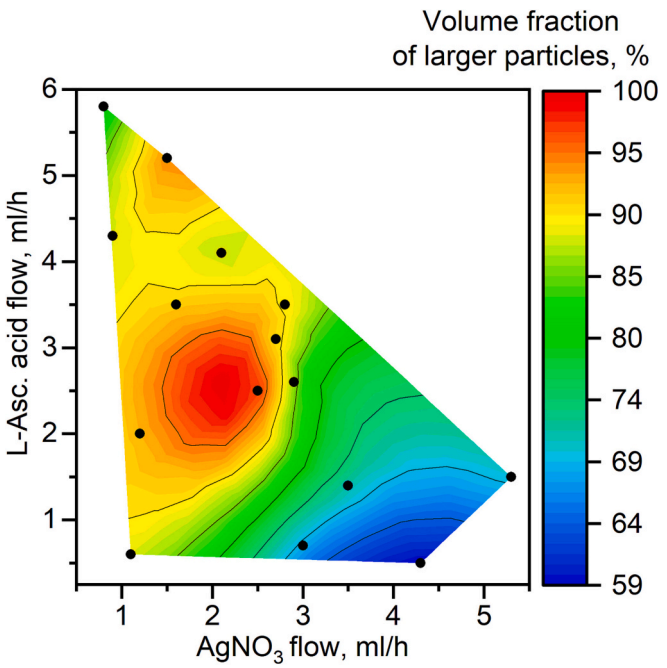

Fig. 7. Colormap representing the volume fraction of Phase 1 with large Ag NPs depending on the ratio between the silver nitrate and ascorbic acid flows, as observed from SAXS. Black dots represent IHS points from the SAXS experiment.

Table 1
Average radius, polydispersity and volume fractions for Ag NP spherical components ("phases") obtained from SAXS data for different synthesis times.

Tube length, cm	Mixing time, s	Average NP radius, nm (polydispersity, nm)		Volume fraction, %	
		Phase 1	Phase 2	Phase 1	Phase 2
8	10	–	–	–	–
40	48	20.0 (7.9)	6.1 (2.1)	17	83
88	107	22.5 (7.3)	6.8 (1.8)	47	53
278	337	23.1 (6.5)	7.2 (2.1)	59	41

with conventional manufacturing technologies.

The surface properties of the microchannels, such as their roughness, hydrophobic/hydrophilic behavior, electrostatic charge, *etc.* play major role in the flow chemistry processes [65,66]. As many common polymer materials used for the MFD fabrication, such as PMMA or PDMS, are naturally hydrophobic, there is vast range of techniques to make their surface hydrophilic and improve adhesion and biocompatibility, like plasma and laser treatment, chemical etching, additional polymer coatings, *etc.* [67–70]. In case of 3D-printed microfluidics, however, situation is quite the opposite. Most of the UV-curable resins used for MSLA/DLP contain hydrophilic, or rather, amphiphilic components. The latter results in so called "contact angle hysteresis" phenomenon, when the channel surface overtime changes its hydrophilic/lipophilic character depending on a liquid being in contact with [71,72]. When in prolonged contact with water, the resin surface dynamically rearranges to expose hydrophilic groups, providing stable wetting of the 3D-printed channels [73]. It is especially critical for aqueous synthesis of nanoparticles, as the metal ions attraction to the rough hydrophilic surface of 3D-printed channels, aggravated by the electrostatic interaction, creates undesirable nucleation centers on the walls of the channel. During continuous flow synthesis in aqueous phase the channels become completely covered with a layer of metal. Several attempts to mitigate this effect were reported so far. They include post-print treatment of the channels with various hydrophobic monomers, surfactants, commercial

Table 2
Combinations of reagent flows, generated by the IHS algorithm and the average radii, polydispersities and volume fractions of the Ag NPs derived from SAXS data.

№	Flow, mL/h			Average NP radius, nm (polydispersity, nm)		Volume fraction, %	
	$AgNO_3$	Na_3Cit	AA	Phase 1	Phase 2	Phase 1	Phase 2
IHS 1	2.5	2.5	2.5	25.1 (9.4)	5.9 (0.5)	98	2
IHS 2	2.7	1.7	3.1	19.6 (5.0)	6.0 (0.5)	91	9
IHS 3	5.3	1	1.5	23.7 (10.0)	4.1 (1.4)	70	30
IHS 4	1.2	4.3	2	20.4 (5.7)	5.9 (0.5)	92	8
IHS 5	1.1	5.8	0.6	19.4 (6.6)	3.9 (0.9)	88	12
IHS 6	1.6	2.4	3.5	16.6 (4.2)	5.9 (0.5)	91	9
IHS 7	0.9	2.3	4.3	17.8 (5.1)	5.8 (0.5)	88	12
IHS 8	0.8	0.9	5.8	30.0 (6.3)	5.7 (0.5)	80	20
IHS 9	1.5	0.8	5.2	26.1 (10.0)	6.3 (0.8)	94	6
IHS 10	2.1	1.3	4.1	23.6 (7.2)	5.7 (0.5)	87	13
IHS 11	2.8	1.2	3.5	25.4 (7.8)	5.7 (0.5)	90	10
IHS 12	3	3.8	0.7	20.2 (7.0)	3.2 (1.1)	68	32
IHS 13	2.9	2	2.6	21.4 (6.5)	5.7 (0.5)	84	16
IHS 14	3.5	2.6	1.4	17.9 (8.0)	3.4 (0.5)	72	28
IHS 15	4.3	2.7	0.5	21.7 (10.0)	3.7 (1.2)	59	41

anti-fog and water repelling agents [74–77]. Some authors attempt modification of commercial 3D-printing resins and even development of new compositions optimized for microfluidic device printing [78–80]. In this work we apply simple approach to make use of the same "contact angle hysteresis" phenomenon that is otherwise harmful for the MFD performance. After printing, cleaning and drying, all microfluidics devices were filled with the same vaseline oil that we use as a carrier phase and left overnight. Prolonged contact with oil exposes oleophilic group on the channel surface and ensures stable wetting, creating thin but persistent oil film. This protective layer prevents nanoparticle growth and precipitation on the channel walls. Droplet synthesis ensures better reaction control and further prevents the contamination of the channels and tubes with reaction products, as their surface is flushed continuously with oil and the protective layer is getting refreshed, allowing for prolonged stable and precise operation of the microfluidic system. The oil also prevents contamination of the UV–Vis cuvette quartz windows and undesirable background buildup, which is highly beneficial for *in situ* characterization. Another important function of the slug flow is to provide mixing of reactants in the water phase as it travels through the system. The initial mixing occurs in the droplet generator chip and in several straight angle turns and channel diameter transitions on the way to the spacer chip [81]. However, majority of the mixing action originates from the nature of the slug flow in the delay line. In the capillary, the water phase moves in oil in a so-called Taylor flow regime [82]. In this regime liquid-capillary and liquid-liquid friction and relative movement create circulatory flows and vortices inside the water slugs, providing fast and reliable mixing [83–85].

The combination of a slug generator with a spacer allows for great flexibility in adjusting droplet size, velocity and spacing. *In situ* characterization with UV–Vis and NIR techniques in working droplet microreactor systems might be challenging in terms of focusing,

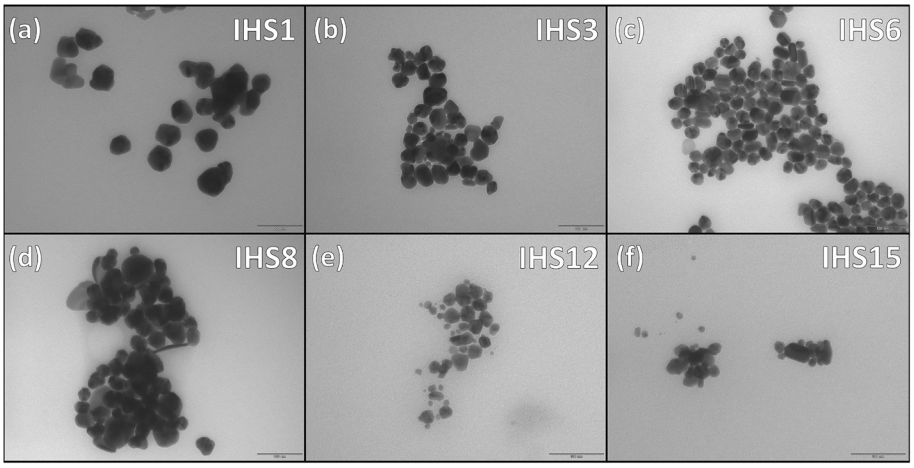

Fig. 8. TEM images of Ag nanoparticles synthesized in microfluidic slugs with selected flow combinations from Table 2.

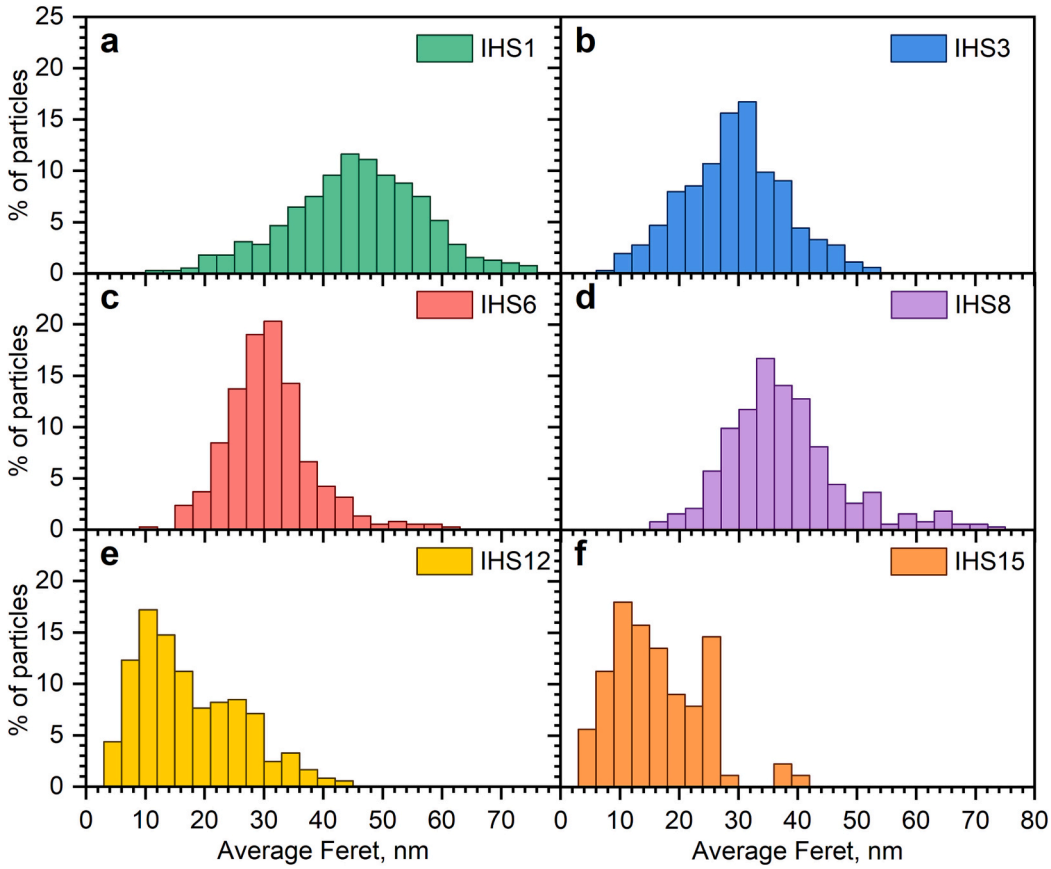

Fig. 9. Average Feret diameter distributions obtained from the TEM images of Ag nanoparticles synthesized in microfluidic slugs with selected flow combinations from Table 2.

synchronization, signal filtration and noise reduction [86,87]. Flexibility of the generator + spacer system allows the user to perfectly tune the segmented flow characteristics to achieve the desired reaction volume, mixing intensity and residence time for various chemical processes [88,89]. It also enables the system adaptation for a selected diagnostics technique, which is otherwise a complex task of creating a proper setup for measurements [90–94]. Use of a 3D-printed cuvette enables easy optimization of its geometry and optical path for different slug flow conditions, solution concentrations and spectrometry setups. In this work, combination of optimized cuvette and sufficient slug volume allowed us to gather high quality spectral data from single slugs. Additionally, the spacer chip facilitates prolonged stability of the slug flow without merging, which is important for long synthesis times, especially at elevated temperatures. It allowed numerous slug trains with different reactant concentrations to reliably co-exist in the delay line in our experimental setup. Thus, we eliminated the need to wait minutes for the end of reaction with one parameter set before proceeding to the next one, dramatically increasing the screening speed.

All the aforementioned benefits are perfectly viable in case of *in situ* synchrotron studies of droplet microreactor synthesis with common X-ray absorption and scattering based techniques. As most beamlines are equipped with setups for quasi-stationary regime, presence of the

continuous phase in droplet flow regime will cause synchronization issues, additional background, and signal quality loss [95–99]. However, working in a slug flow with sufficiently long slugs provides sufficient time for measurements in continuous acquisition mode for easy synchrotron diagnostics, and even allows to simply measure scattering and absorption in slugs directly through the PTFE or FEP tube without the need for *in situ* cell.

However, efficient experimental data collection is only a part of the job. It is just as important to be able to efficiently analyze it. Since recent, machine learning methods gradually became a new meta in material science for solving complex data analysis problems, finding concealed correlations and predicting new materials and their properties [100,101]. With the right set of descriptors, it has an advantage of being able to process arbitrary and natural data without specific knowledge or scientific insights, so it can be applied with equal success to analyze spectral, imaging, statistical information, *etc.* for a variety of applications and material classes [102–105]. This makes ML a particularly powerful instrument for high-throughput screening and exploration of materials and chemical reactions, as it does not care about the specifics of the actual chemistry being studied or experimental methods being used for the characterization [106–110]. However, training reliable ML models requires relevant and well-distributed dataset with a good coverage. In this work we demonstrate that the microfluidics combined with *in situ* characterization is a versatile tool for rapid, automated and low-cost creation of such a dataset. However, it is also crucial to properly choose specific ML algorithms used for the training. The combination of efficient IHS sampling algorithm and Extra Trees Regressor that we use in this work proves to be very powerful for limited size datasets, being able to train better models in terms of generalization and reliability to dataset size ratio, compared to other ML algorithms applied to the similar problem [111–113].

5. Conclusions

Efficient optimization of microfluidic synthesis requires *in situ* diagnostics and online data processing. In our work we demonstrate simple and versatile system based on 3D-printed microfluidic components. DLP-SLA technology allows to easily manufacture microfluidic devices tailored to a specific needs, such as mixing, water-in-oil slug generation and spacing, *in situ* cells for UV–Vis spectroscopy and SAXS. Oil soaking of 3D-printed chips improves hydrophobicity of channel surface, and use of the slug flow further prevents nanoparticle growth on the channel walls and cuvette windows. Use of sufficiently long slugs and optimized optical path in the cuvette allows to obtain high-quality *in situ* optical spectroscopy data in a single shot from a single slug, enabling the ability to test dozens of combinations of parameters per hour. For synchrotron studies it allows to obtain *in situ* data from slugs directly through a FEP tube in quasi-stationary regime, without the need for a microfocus beam and synchronization.

The proposed system, combined with automated experiment control software and IHS-based sampling algorithm allows rapid and efficient screening of microfluidic reaction parameters. In this paper we demonstrated application of this approach to study the relationships between Ag nanoparticle optical properties, size distribution and reaction parameters. Using *in situ* UV–Vis absorption spectroscopy and SAXS we were able to quickly screen the impact of synthesis conditions on surface plasmon resonance properties, growth time, size and polydispersity of Ag nanoparticles. ML models were further trained on the *in situ* UV–Vis data and demonstrated high prediction quality. The trained algorithm can be applied for the inverse problem to predict the experimental parameters required to obtain NPs with given spectral response. As an example, we were able to conclude that in our setup the most monodisperse NPs with the strongest LSPR red-shifted peak should be obtained with nearly stochiometric ascorbic acid and silver nitrate ratio with slight AA excess, which was further validated by SAXS measurements. We believe that the approach based on a 3D-printed microfluidic devices optimized for conventional *in situ* spectroscopic characterization will heavily increase the throughput of material diagnostics in laboratories and synchrotrons and accelerate the development of new functional nanomaterials.

Declaration of Competing Interest

The authors declare that they have no known competing financial interests or personal relationships that could have appeared to influence the work reported in this paper.

Data availability

Data will be made available on request.

Acknowledgements

The authors acknowledge the Ministry of Science and Higher Education of the Russian Federation for financial support (Agreement no. 075-15-2021-1363).

Appendix A. Supplementary data

Supplementary data to this article can be found online at https://doi.org/10.1016/j.mne.2023.100224.

References

[1] S.M. Mousavi, et al., Green synthesis of silver nanoparticles toward bio and medical applications: review study, Artif. Cells, Nanomed. Biotechnol. 46 (3) (2018) 855–872.
[2] M.A. Shenashen, S.A. El-Safty, E.A. Elshehy, Synthesis, morphological control, and properties of silver nanoparticles in potential applications, Part. Part. Syst. Charact. 31 (3) (2014) 293–316.
[3] G. Habibullah, J. Viktorova, T. Ruml, Current strategies for noble metal nanoparticle synthesis, Nanoscale Res. Lett. 16 (1) (2021) 47.
[4] N.D. Burrows, et al., Understanding the seed-mediated growth of gold nanorods through a fractional factorial design of experiments, Langmuir 33 (8) (2017) 1891–1907.
[5] T. Pretto, et al., Design of experiments a powerful tool to improve the selectivity of copper antimony sulfide nanoparticles synthesis, CrystEngComm 23 (2) (2021) 397–403.
[6] K. Abdel-Latif, et al., Self-driven multistep quantum dot synthesis enabled by autonomous robotic experimentation in flow, Adv. Intel. Syst. 3 (2) (2021) 2000245.
[7] M. Tavares Luiz, et al., Design of experiments (DoE) to develop and to optimize nanoparticles as drug delivery systems, Eur. J. Pharm. Biopharm. 165 (2021) 127–148.
[8] H. Tao, et al., Nanoparticle synthesis assisted by machine learning, Nat. Rev. Mater. 6 (8) (2021) 701–716.
[9] E.J. Braham, et al., Machine learning-directed navigation of synthetic design space: a statistical learning approach to controlling the synthesis of perovskite halide nanoplatelets in the quantum-confined regime, Chem. Mater. 31 (9) (2019) 3281–3292.
[10] O. Voznyy, et al., Machine learning accelerates discovery of optimal colloidal quantum dot synthesis, ACS Nano 13 (10) (2019) 11122–11128.
[11] B. Dong, et al., Synthesis of monodisperse spherical AgNPs by ultrasound-intensified Lee-Meisel method, and quick evaluation via machine learning, Ultrason. Sonochem. 73 (2021), 105485.
[12] J. Li, et al., Deep learning accelerated gold nanocluster synthesis, Adv. Intel. Syst. 1 (3) (2019) 1900029.
[13] H. Zhao, et al., A robotic platform for the synthesis of colloidal nanocrystals, Nat. Synthesis 2 (2023) 505–514.
[14] C.B. Wahl, et al., Machine learning–accelerated design and synthesis of polyelemental heterostructures, Sci. Adv. 7 (52) (2021) eabj5505.
[15] F. Pellegrino, et al., Machine learning approach for elucidating and predicting the role of synthesis parameters on the shape and size of TiO2 nanoparticles, Sci. Rep. 10 (1) (2020) 18910.
[16] G.M. Whitesides, The origins and the future of microfluidics, Nature 442 (7101) (2006) 368–373.
[17] P. Shrimal, G. Jadeja, S. Patel, A review on novel methodologies for drug nanoparticle preparation: microfluidic approach, Chem. Eng. Res. Des. 153 (2020) 728–756.
[18] V. Sans, L. Cronin, Towards dial-a-molecule by integrating continuous flow, analytics and self-optimisation, Chem. Soc. Rev. 45 (8) (2016) 2032–2043.

[19] D.C. Fabry, E. Sugiono, M. Rueping, Online monitoring and analysis for autonomous continuous flow self-optimizing reactor systems, React. Chem. Eng. 1 (2) (2016) 129–133.
[20] J. Yue, J.C. Schouten, T.A. Nijhuis, Integration of microreactors with spectroscopic detection for online reaction monitoring and catalyst characterization, Ind. Eng. Chem. Res. 51 (45) (2012) 14583–14609.
[21] J. Ji, et al., Surface plasmon resonance tuning in gold film on silver nanospheres through optical absorption, Sens. Bio-Sens. Res. 30 (2020), 100374.
[22] L.A. Austin, et al., The optical, photothermal, and facile surface chemical properties of gold and silver nanoparticles in biodiagnostics, therapy, and drug delivery, Arch. Toxicol. 88 (7) (2014) 1391–1417.
[23] C. Le, et al., Searching for high similarity of longitudinal local surface plasmon resonance in gold and silver nanobipyramids, Mater. Today Commun. 30 (2022) 103173.
[24] A.R. Tao, S. Habas, P. Yang, Shape control of colloidal metal nanocrystals, Small 4 (3) (2008) 310–325.
[25] H.V. Nguyen, et al., Serially diluting centrifugal microfluidics for high-throughput gold nanoparticle synthesis using an automated and portable workstation, Chem. Eng. J. 452 (2023), 139044.
[26] Z. Yang, et al., Controllable synthesis of silver nanoparticles using a multi-stage microfluidic reactor driven by two valveless piezoelectric pumps, Sensors Actuators A Phys. 346 (2022), 113871.
[27] M. Chen, et al., A dual-angle fiber dynamic light scattering system integrated with microfluidic chip for particle size measurement, Opt. Laser Technol. 150 (2022), 107891.
[28] D. McIntyre, et al., Machine learning for microfluidic design and control, Lab Chip 22 (16) (2022) 2925–2937.
[29] F. Mekki-Berrada, et al., Two-step machine learning enables optimized nanoparticle synthesis, npj Comp. Mater. 7 (1) (2021) 55.
[30] R.M. Maceiczyk, A.J. deMello, Fast and reliable metamodeling of complex reaction spaces using universal kriging, J. Phys. Chem. C 118 (34) (2014) 20026–20033.
[31] S. Li, et al., Automated microfluidic screening of ligand interactions during the synthesis of cesium lead bromide nanocrystals, Mol. Syst. Design Eng. 5 (6) (2020) 1118–1130.
[32] A. Yaghmur, I. Hamad, Microfluidic nanomaterial synthesis and in situ SAXS, WAXS, or SANS characterization: manipulation of size characteristics and online elucidation of dynamic structural transitions, Molecules 27 (14) (2022) 4602.
[33] E. Ilhan-Ayisigi, et al., Advances in microfluidic synthesis and coupling with synchrotron SAXS for continuous production and real-time structural characterization of nano-self-assemblies, Colloids Surf. B: Biointerfaces 201 (2021), 111633.
[34] D. Radajewski, et al., An innovative data processing method for studying nanoparticle formation in droplet microfluidics using X-rays scattering, Lab Chip 21 (22) (2021) 4498–4506.
[35] T. Lange, et al., OSTE+ for in situ SAXS analysis with droplet microfluidic devices, Lab Chip 20 (16) (2020) 2990–3000.
[36] K. Ren, J. Zhou, H. Wu, Materials for microfluidic chip fabrication, Acc. Chem. Res. 46 (11) (2013) 2396–2406.
[37] J. Hwang, et al., Microchannel fabrication on glass materials for microfluidic devices, Int. J. Precis. Eng. Manuf. 20 (3) (2019) 479–495.
[38] A. Olanrewaju, et al., Capillary microfluidics in microchannels: from microfluidic networks to capillaric circuits, Lab Chip 18 (16) (2018) 2323–2347.
[39] M. Zeraatkar, D. Filippini, G., Percoco on the impact of the fabrication method on the performance of 3D printed mixers, Micromachines 10 (2019), https://doi.org/10.3390/mi10050298.
[40] G. Weisgrab, A. Ovsianikov, P.F. Costa, Functional 3D printing for microfluidic chips, Adv. Mater. Technol. 4 (10) (2019) 1900275.
[41] N.P. Macdonald, et al., Comparing microfluidic performance of three-dimensional (3D) printing platforms, Anal. Chem. 89 (7) (2017) 3858–3866.
[42] G. Gonzalez, et al., Current and emerging trends in polymeric 3D printed microfluidic devices, Add. Manufact. 55 (2022), 102867.
[43] K. Griffin, D. Pappas, 3D printed microfluidics for bioanalysis: a review of recent advancements and applications, TrAC Trends Anal. Chem. 158 (2023), 116892.
[44] A.A. Guda, et al., Machine learning analysis of reaction parameters in UV-mediated synthesis of gold nanoparticles, J. Phys. Chem. C 127 (2) (2023) 1097–1108.
[45] P.J.E.M. van der Linden, A.M. Popov, D. Pontoni, Accurate and rapid 3D printing of microfluidic devices using wavelength selection on a DLP printer, Lab Chip 20 (22) (2020) 4128–4140.
[46] L.P. Bressan, et al., 3D-printed microfluidic device for the synthesis of silver and gold nanoparticles, Microchem. J. 146 (2019) 1083–1089.
[47] R.M. Camarillo-Escobedo, et al., 3D printed opto-microfluidic autonomous analyzer for photometric applications, Sensors Actuators A Phys. 337 (2022), 113425.
[48] B. Beachkofski, R. Grandhi, Improved distributed hypercube sampling, in: In 43rd AIAA/ASME/ASCE/AHS/ASC Structures, Structural Dynamics, and Materials Conference, American Institute of Aeronautics and Astronautics, 2002.
[49] G.S. Peters, et al., The small-angle X-ray scattering beamline BioMUR at the Kurchatov synchrotron radiation source, Nuclear Instruments Methods Phys. Res. Section A: Accelerat. Spectrom. Detect. Assoc. Equip. 945 (2019), 162616.
[50] A.P. Hammersley, et al., Two-dimensional detector software: from real detector to idealised image or two-theta scan, High Pressure Res. 14 (4–6) (1996) 235–248.
[51] P.V. Konarev, et al., PRIMUS: a windows PC-based system for small-angle scattering data analysis, J. Appl. Crystallogr. 36 (5) (2003) 1277–1282.
[52] T.J. Collins, ImageJ for microscopy, BioTechniques 43 (1S) (2007) S25–S30.
[53] Particle size, size distributions and shape, in: H.G. Merkus, H.G. Merkus (Eds.), Particle Size Measurements: Fundamentals, Practice, Quality, Springer Netherlands, Dordrecht, 2009, pp. 13–42.
[54] P. Geurts, D. Ernst, L. Wehenkel, Extremely randomized trees, Mach. Learn. 63 (1) (2006) 3–42.
[55] F. Pedregosa, et al., Scikit-learn: machine learning in Python, J. Mach. Learn. Res. 12 (2011) 2825–2830.
[56] A. Martini, et al., PyFitit: the software for quantitative analysis of XANES spectra using machine-learning algorithms, Comput. Phys. Commun. 250 (2020), 107064.
[57] I. Sondi, D.V. Goia, E. Matijević, Preparation of highly concentrated stable dispersions of uniform silver nanoparticles, J. Colloid Interface Sci. 260 (1) (2003) 75–81.
[58] Y. Qin, et al., Size control over spherical silver nanoparticles by ascorbic acid reduction, Colloids Surf. A Physicochem. Eng. Asp. 372 (1) (2010) 172–176.
[59] L. Marciniak, et al., The effect of pH on the size of silver nanoparticles obtained in the reduction reaction with citric and malic acids, Materials (2020) 13, https://doi.org/10.3390/ma13235444.
[60] L. Malassis, et al., One-step green synthesis of gold and silver nanoparticles with ascorbic acid and their versatile surface post-functionalization, RSC Adv. 6 (39) (2016) 33092–33100.
[61] K.P. Velikov, G.E. Zegers, A. van Blaaderen, Synthesis and characterization of large colloidal silver particles, Langmuir 19 (4) (2003) 1384–1389.
[62] L. Xu, et al., Droplet synthesis of silver nanoparticles by a microfluidic device, Chem. Eng. Process. Process Intensif. 102 (2016) 186–193.
[63] O. Kašpar, et al., Governing factors for preparation of silver nanoparticles using droplet-based microfluidic device, Biomed. Microdevices 21 (4) (2019) 88.
[64] X. Dong, et al., Shape control of silver nanoparticles by stepwise citrate reduction, J. Phys. Chem. C 113 (16) (2009) 6573–6576.
[65] S.K. Mitra, A.A. Saha, Surface modification, methods, in: D. Li (Ed.), Encyclopedia of Microfluidics and Nanofluidics, Springer US, Boston, MA, 2008, pp. 1933–1939.
[66] T. Kawakatsu, et al., The effect of the hydrophobicity of microchannels and components in water and oil phases on droplet formation in microchannel water-in-oil emulsification, Colloids Surf. A Physicochem. Eng. Asp. 179 (1) (2001) 29–37.
[67] Hong, S.M., et al. Hydrophilic Surface Modification of PDMS using Atmospheric RF Plasma. IOP Publishing.
[68] H. Makamba, et al., Surface modification of poly (dimethylsiloxane) microchannels, Electrophoresis 24 (21) (2003) 3607–3619.
[69] T. Trantidou, et al., Hydrophilic surface modification of PDMS for droplet microfluidics using a simple, quick, and robust method via PVA deposition, Microsyst. Nanoeng. 3 (1) (2017) 16091.
[70] M.T. Khorasani, H. Mirzadeh, P.G. Sammes, Laser surface modification of polymers to improve biocompatibility: HEMA grafted PDMS, in vitro assay—III, Radiat. Phys. Chem. 55 (5–6) (1999) 685–689.
[71] F.J.M. Ruiz-Cabello, M.A. Rodríguez-Valverde, M.A. Cabrerizo-Vilchez, Contact angle hysteresis on polymer surfaces: an experimental study, J. Adhes. Sci. Technol. 25 (16) (2011) 2039–2049.
[72] L. Gao, T.J. McCarthy, Contact angle hysteresis explained, Langmuir 22 (14) (2006) 6234–6237.
[73] O.N. Tretinnikov, Y. Ikada, Dynamic wetting and contact angle hysteresis of polymer surfaces studied with the modified Wilhelmy balance method, Langmuir 10 (5) (1994) 1606–1614.
[74] C. Cheng, M. Gupta, Surface functionalization of 3D-printed plastics via initiated chemical vapor deposition, Beilstein J. Nanotechnol. 8 (2017) 1629–1636.
[75] C.A. Warr, et al., Surface modification of 3D printed microfluidic devices for controlled wetting in two-phase flow, Micromachines 14 (2023), https://doi.org/10.3390/mi14010006.
[76] K. Ohtani, et al., Surface treatment of flow channels in microfluidic devices fabricated by stereolithography, J. Oleo. Sci. 63 (1) (2014) 93–96.
[77] A. Amini, et al., Recent developments in digital light processing 3D-printing techniques for microfluidic analytical devices, J. Chromatogr. A 1692 (2023), 463842.
[78] C.A. Warr, et al., 3D-printed microfluidic droplet generator with hydrophilic and hydrophobic polymers, Micromachines 12 (2021), https://doi.org/10.3390/mi12010091.
[79] X. Wang, et al., i3DP, a robust 3D printing approach enabling genetic post-printing surface modification, Chem. Commun. 49 (86) (2013) 10064–10066.
[80] M.J. Männel, et al., Combining hydrophilic and hydrophobic materials in 3D printing for fabricating microfluidic devices with spatial wettability, Adv. Mater. Technol. 6 (9) (2021) 2100094.
[81] S. Zhao, et al., Three-dimensional simulation of mixing performance inside droplets in micro-channels by lattice Boltzmann method, Chem. Eng. J. 207-208 (2012) 267–277.
[82] Z. Peng, et al., A review of microreactors based on slurry Taylor (segmented) flow, Chem. Eng. Sci. 247 (2022), 117040.
[83] M.N. Kashid, A. Renken, L. Kiwi-Minsker, Gas–liquid and liquid–liquid mass transfer in microstructured reactors, Chem. Eng. Sci. 66 (17) (2011) 3876–3897.
[84] L. Yang, M.J. Nieves-Remacha, K.F. Jensen, Simulations and analysis of multiphase transport and reaction in segmented flow microreactors, Chem. Eng. Sci. 169 (2017) 106–116.
[85] C. Yao, et al., Mass transfer in liquid-liquid Taylor flow in a microchannel: local concentration distribution, mass transfer regime and the effect of fluid viscosity, Chem. Eng. Sci. 223 (2020), 115734.

[86] D.E.W. Patabadige, et al., Micro total analysis systems: fundamental advances and applications, Anal. Chem. 88 (1) (2016) 320–338.
[87] T. Jurina, et al., Application of spectroscopy techniques for monitoring (bio) catalytic processes in continuously operated microreactor systems, Catalysts 13 (2023), https://doi.org/10.3390/catal13040690.
[88] W. Tanthapanichakoon, et al., Design of mixing in microfluidic liquid slugs based on a new dimensionless number for precise reaction and mixing operations, Chem. Eng. Sci. 61 (13) (2006) 4220–4232.
[89] C. Yao, et al., Formation of liquid–liquid slug flow in a microfluidic T-junction: effects of fluid properties and leakage flow, AICHE J. 64 (1) (2018) 346–357.
[90] J. Yue, et al., Microreactors with integrated UV/Vis spectroscopic detection for online process analysis under segmented flow, Lab Chip 13 (24) (2013) 4855.
[91] K.L.A. Chan, S.G. Kazarian, FT-IR spectroscopic imaging of reactions in multiphase flow in microfluidic channels, Anal. Chem. 84 (9) (2012) 4052–4056.
[92] P.C. Ashok, et al., Waveguide confined Raman spectroscopy for microfluidic interrogation, Lab Chip 11 (7) (2011) 1262–1270.
[93] N. Steinfeldt, U. Bentrup, K. Jähnisch, Reaction mechanism and in situ ATR spectroscopic studies of the 1-decene ozonolysis in micro- and semibatch reactors, Ind. Eng. Chem. Res. 49 (1) (2010) 72–80.
[94] A. Urakawa, et al., On-chip Raman analysis of heterogeneous catalytic reaction in supercritical CO2: phase behaviour monitoring and activity profiling, Analyst 133 (10) (2008) 1352–1354.
[95] J. Probst, et al., In situ X-ray absorption spectroscopy and droplet-based microfluidics: an analysis of calcium carbonate precipitation, ACS Measure. Sci. Au 1 (1) (2021) 27–34.
[96] J. Xto, et al., Droplet-based in situ X-ray absorption spectroscopy cell for studying crystallization processes at the tender X-ray energy range, RSC Adv. 9 (58) (2019) 34004–34010.
[97] M. Nagasaka, et al., Laminar flow in microfluidics investigated by spatially-resolved soft X-ray absorption and infrared spectroscopy, J. Chem. Phys. 151 (11) (2019) 114201.
[98] M.A. Levenstein, et al., Droplet microfluidics XRD identifies effective nucleating agents for calcium carbonate, Adv. Funct. Mater. 29 (19) (2019) 1808172.
[99] A. Ghazal, et al., Recent advances in X-ray compatible microfluidics for applications in soft materials and life sciences, Lab Chip 16 (22) (2016) 4263–4295.
[100] J. Fang, et al., Machine learning accelerates the materials discovery, Mater. Today Commun. 33 (2022), 104900.
[101] Y. Juan, et al., Accelerating materials discovery using machine learning, J. Mater. Sci. Technol. 79 (2021) 178–190.
[102] M. Hu, et al., Recent applications of machine learning in alloy design: a review, Mater. Sci. Eng. R. Rep. 155 (2023), 100746.
[103] J. Lin, et al., Machine learning accelerates the investigation of targeted MOFs: performance prediction, rational design and intelligent synthesis, Nano Today 49 (2023), 101802.
[104] J.C.A. Oliveira, et al., When machine learning meets molecular synthesis, Trends Chem. 4 (10) (2022) 863–885.
[105] Y. Qiu, et al., Machine learning promotes the development of all-solid-state batteries, Chinese J. Struct. Chem. (2023) 100118.
[106] D. Packwood, et al., Machine learning in materials chemistry: an invitation, Mach. Learn. Appl. 8 (2022), 100265.
[107] K. Batalović, et al., Machine learning-based high-throughput screening of Mg-containing alloys for hydrogen storage and energy conversion applications, J. Energy Stor. 68 (2023), 107720.
[108] Y. Du, et al., ATR-FTIR combined with machine learning for the fast non-targeted screening of new psychoactive substances, Forensic Sci. Int. 349 (2023), 111761.
[109] K.M. Katubi, et al., Machine learning assisted designing of organic semiconductors for organic solar cells: high-throughput screening and reorganization energy prediction, Inorg. Chem. Commun. 151 (2023), 110610.
[110] X. Zhang, et al., Machine learning screening of high-performance single-atom electrocatalysts for two-electron oxygen reduction reaction, J. Colloid Interface Sci. 645 (2023) 956–963.
[111] K. Nathanael, et al., Optimization of microfluidic synthesis of silver nanoparticles: a generic approach using machine learning, Chem. Eng. Res. Des. 193 (2023) 65–74.
[112] T. Kashiwagi, et al., High-throughput synthesis of silver nanoplates and optimization of optical properties by machine learning, Chem. Eng. Sci. 262 (2022), 118009.
[113] J. Park, et al., Closed-loop optimization of nanoparticle synthesis enabled by robotics and machine learning, Matter 6 (3) (2023) 677–690.